IEEE Photonics Journal
An IEEE Photonics Society Publication

Open Access

A Novel Birefrigent Photonic Crystal Fiber Surface Plasmon Resonance Biosensor

Volume 6, Number 4, August 2014

R. Otupiri
E. K. Akowuah
S. Haxha, Senior Member, IEEE
H. Ademgil
F. AbdelMalek
A. Aggoun

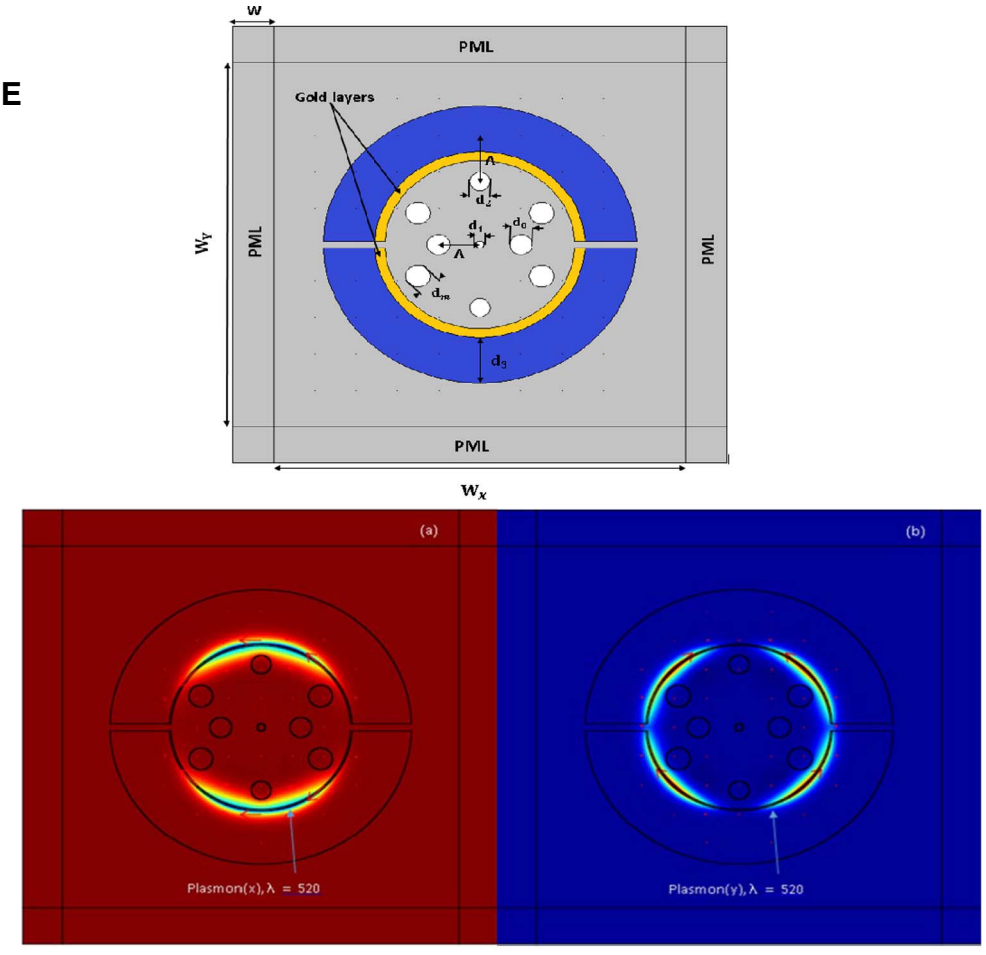

Schematic diagram of the Photonic Crystal SPR Biosensor with the Magnetic Distribution of Plasmon Modes on Gold Surface

DOI: 10.1109/JPHOT.2014.2335716
1943-0655

IEEE photonics SOCIETY

IEEE

A Novel Birefrigent Photonic Crystal Fiber Surface Plasmon Resonance Biosensor

R. Otupiri,[1] E. K. Akowuah,[2] S. Haxha,[3,5] *Senior Member, IEEE*, H. Ademgil,[4] F. AbdelMalek,[3] and A. Aggoun[5]

[1]Department of Electrical & Electronic Eng., Kwame Nkrumah University of Science and Technology, Kumansi 00233, Ghana,
[2]Department of Computer Eng., Kwame Nkrumah University of Science and Technology, Kumansi 00233, Ghana,
[3]School of Electronics and Digital Arts, University of Kent, Kent CT2 7NJ, U.K.
[4]Department of Electronics, European University of Lefke, Lefke Mersin 10, Turkey
[5]Department of Computer Science and Technologies, University of Bedfordshire, Bedfordshire LU1 3JU, U.K.

DOI: 10.1109/JPHOT.2014.2335716

Manuscript received May 29, 2014; revised June 25, 2014; accepted June 26, 2014. Date of publication July 8, 2014; date of current version July 14, 2014. Corresponding author: S. Haxha (e-mail: Shyqyri.Haxha@beds.ac.uk).

Abstract: A numerical analysis of a novel birefringent photonic crystal fiber (PCF) biosensor constructed on the surface plasmon resonance (SPR) model is presented in this paper. This biosensor configuration utilizes circular air holes to introduce birefringence into the structure. This PCF biosensor model shows promise in the area of multiple detection using HE_{11}^{x} and HE_{11}^{y} modes to sense more than one analyte. A numerical study of the biosensor is performed in two interrogation modes: amplitude and wavelength. Sensor resolution values with spectral interrogation yielded 5×10^{-5} RIU (refractive index units) for HE_{11}^{x} modes and 6×10^{-5} RIU for HE_{11}^{y} modes, whereas 3×10^{-5} RIU for HE_{11}^{x} modes and 4×10^{-5} RIU for HE_{11}^{y} modes are demonstrated for the amplitude interrogation.

Index Terms: Surface plasmon, photonic crystal fiber, biosensor, fiber optic sensors.

1. Introduction

In recent years, surface plasmon resonance (SPR) sensing has been accepted to be a robust and effective method of direct sensing [1]. Presently, SPR based sensing technique is by far the most advanced form of real time label free sensing. It has been used extensively in the study of biomolecular interactions (BIA) and in the recognition of target analytes, both chemical and biological [1]–[3]. It is has therefore found several applications in the areas of food safety, biochemical technology, medicine, and other daily-life applications [4].

Many present day SPR biosensors on the market are based on the traditional prism-coupled configuration. The largesize and the existence of several optical and mechanical components make optimization and commercial production of prism based sensors on a large scale difficult [5]. In addition, they cannot easily be miniaturized or incorporated into other systems [6], [7], resulting in the need to develop compact, robust and highly sensitive SPR biosensors that can be used for measurements outside a laboratory [2], [3], [7]–[10].

In recent times, various compact structures allowing coupling of optical waveguide modes and surface plasmon waveshave been reported: metallized single-mode, lapped D-shaped fiber

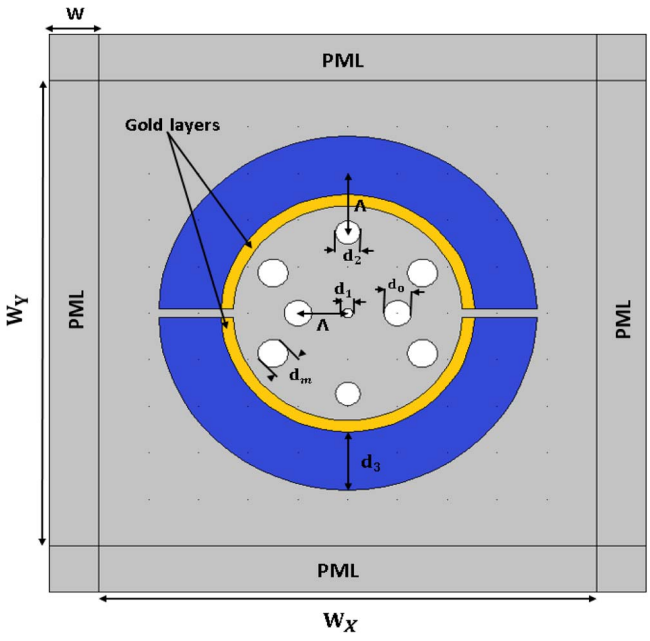

Fig. 1. Schematic diagram of the PCF biosensor showing all sections.

sensors, polarization maintaining, metallized tapered fibers [13]–[15], and, recently, PCF employing elliptical air holes with metallic slots [16]. Fiber optic SPR biosensors are compact, offer multiplexing, remote sensing and device miniaturization [14]–[16]. These designs are focused on the coupling of a leaky fundamental mode to the surface plasmon polaritons (SPP), which are surface electromagnetic excitation on the metal layer in the micro-structure [17].

PCFs, also known as holey fibers, are fabricated from a sole substrate such as glass with an even distribution oftiny holes along the fiber length [18]. The introduction of PCFs has opened up new possibilities, some of which are light guidance through vacuum, unusual dispersion properties, high confinement of light and tunable non-linear effects [19], [20]. Such unique characteristics of PCFs have sparked growing interest intheir use in fields such as high power applications, signal processing, and sensing. As a result, various types of SPR based microstructured optical fiber (MOF) sensors and photonic bandgap SPR sensors have been proposed [22]–[25].

In this paper, we report a numerical study on a novel highly birefringent PCF biosensor based on SPR, optimized tofunction in aquatic environments. Fig. 1 shows the structure of the proposed SPR sensor. It is composed of asmall air hole in the center to aid coupling between guided and plasmon modes, two metallized micro fluidic slots and a number of are holes of varying diameters for guiding the light. Investigation of key performance parameters for example, birefringence, confinement loss, and sensitivity, was achieved using a full-vectorial Finite Element Method (FEM), with anisotropic (PML) Perfectly Matched Layers.

With regard to sensitivity, the proposed SPR biosensor is comparable to those in [4] and [5]. Furthermore, fabrication of the structure should not be much of a problemdue to the few air holes and large channels for housing the analyte. The thin gold layer on the inner surfaces of the micro fluidic slots can be achieved using high pressure chemical vapor deposition technique, thermal evaporation, or a sputtering method [26]. Alternatively, electroless plating techniques used in fabrication of metallized hollow waveguides and microstructures can also be employed to deposit the required amount of gold [27], [28].

2. Theory

The cross section of the PCF depicted in Fig. 1 is divided into a mesh of triangular subspaces within each of Maxwell's equations is solved, taking into account neighboring subspaces using

FEM. Triangular subspaces represent circular structures better than any other, hence the reason for their use in this case [20], [29], [30]. The following is the vectorial wave equation derived from Maxwell's equations [20], [22]–[30]:

$$\nabla \times \left([s]^{-1}\nabla \times E\right) - k_0^2 n^2 [] E = 0 \tag{1}$$

where [s] represents the PML 3× 3 matrix, $[s]^{-1}$ is the inverse of [s] matrix, $k_0(=2\pi/\lambda)$ is the wave number in vacuum, E is the electric field vector, n is the refractive index of the domain and λ represents the operating wavelength, and the propagating constant β is

$$\beta = n_{eff} k_0 \tag{2}$$

where n_{eff} is the effective index of the mode. If $\lambda = \lambda_0$, the wavelength in a vacuum, then

$$\beta = \frac{2\pi}{\lambda_0} n_{eff} = \frac{2\pi}{\frac{\lambda_0}{n}} = \frac{2\pi}{\lambda_{eff}} \tag{3}$$

where $\lambda_{eff} = \lambda_0/n_{eff}$ is the z-directional component of the wavelength in the medium, and β (the propagation constant) is the phase rotation per unitdistance. The effective index n_{eff} is the ratio of a wavelength in a given medium to that in a vacuum or as the ratio of a phase rotation in a medium to that in a vacuum.

The propagation constant of a surface plasmon wave (SPW) such a wave is defined as

$$\beta_{spw} = \frac{\omega}{c}\sqrt{\frac{\varepsilon_m \varepsilon}{\varepsilon_m + \varepsilon_d}} \tag{4}$$

where ω, c, ε_m, and ε_d represent the angular frequency, the speed oflight in vacuum and the dielectric functions of the metal and dielectric, respectively [1].

In waveguides, coupling of the core mode to the plasmon mode at phase matching excites the SPW on the metal surface. Mathematically, the effective indices of the two modes at a given wavelength of operation are equal [23].

Sensing the change in the confinement loss of the PCF when the core-guided mode is coupled to the plasmon mode at the phase matching point is the underlying detection mechanism for most sensor designs. In the following equation, confinement loss calculations utilize the imaginary part of the complex refractive index n_{eff} [20]:

$$\frac{40\pi}{\ln(10)\lambda} \mathrm{Im}(n_{eff}) \times 10^4 \approx 8.686_0 \mathrm{Im}(n_{eff}) \times 10^4 \ [\mathrm{dB/cm}]. \tag{5}$$

3. Simulation and Results

The proposed PCF biosensor, as illustrated in Fig. 1, is composed of a hexagonal lattice of circular air holes of varyingradii and a central tiny air hole. The large circular air holes, denoted by d_m, are used to introduce birefringence into the structure. Tuning of the phase matching point of the core mode to the plasmon mode is achieved with the small circular hole at the center of the structure denoted byd_1. The presence of d_1 at the center of the structure reduces the refractive index in central core area. The pitch, denoted by Λ, is the inter air hole spacing. The two holes in the first ring distort the perfect symmetry of the guided core mode thereby introducing birefringence into the module. The four large holes in the second ring are used to vary the amount of birefringence being introduced. Additionally, the second ring forms a cladding with low refractive index which enables wave guidance. The third ring is composed of two gold coated slots of same thickness d_3 which house the analyte.

Throughout this study the slot gap d_s is set equal to d_1. The birefringent nature of the SPR based PCF sensor requires this channel design to provide enough coverage for the two

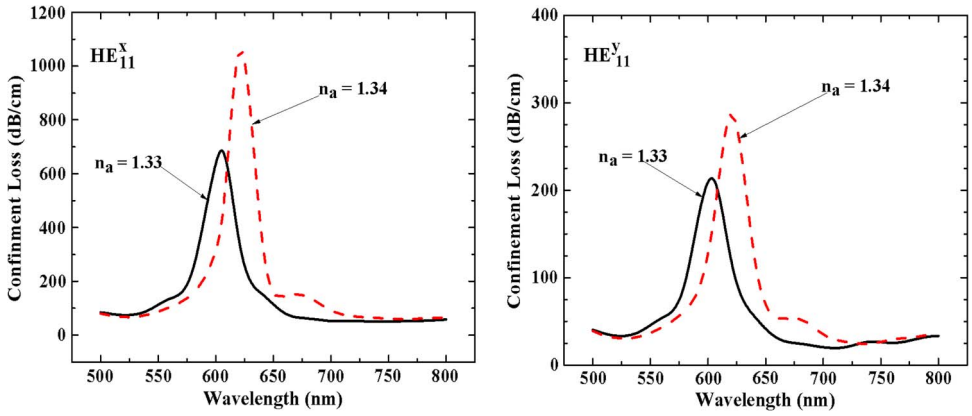

Fig. 2. Loss spectra of x and y polarizations of the fundamental modes (HE^x_{11} and HE^y_{11}). Attenuation peaks for both solid ($n_a = 1.33$) and dash ($n_a = 1.34$) curves correspond to excited plasmons on the gold surface.

polarized modes. The slots have gold layers (thickness t_{Au}) on which the surface plasmon would be excited. The Sellmeier equation is used to model the background material (silica) [31]

$$n(\lambda) = \sqrt{1 + \frac{B_1\lambda^2}{\lambda^2 - C_1} + \frac{{}_2\lambda^2}{\lambda^2 - C_2} + \frac{B_3\lambda^2}{\lambda^2 - {}_3}} \tag{6}$$

where n is the index of refraction, and $\lambda(\mu m)$ is wavelength, with $B_{(i=1,2,3)}$ and $C_{(i=1,2,3)}$ as Sellmeier coefficients. The values of the coefficients are defined as follows: $B_1 = 0.696166300$, $B_2 = 0.407942600$, $B_3 = 0.897479400$, $C_1 = 4.67914826 \times 10^{-3}\ \mu m^2$, $C_2 = 1.35120631 \times 10^{-2}\ \mu m^2$, and $C_3 = 97.9340025\ \mu m^2$ [29]. Gold permittivity is modeled from Johnson and Christy data [32].

Full vectorial FEM is employed in all simulations. The schematic of the PCF SPR biosensor model is divided into triangular pieces forming a mesh. In this way, accurate representation of the step index profile is achieved. The solver settings of FEM based on anisotropic perfectly matched layers (PML) enable any desired number of confined and leaky modes to be analyzed. PML as a boundary condition enables accurate analysis leaky modes propagating through [30]. The primary focus of the study is the fundamental modes HE^x_{11} and HE^y_{11}. Since the wave propagates in the zdirection, modal analysis of the fundamental mode has been performed in the x–y plane of the cross section.

Our analysis begins with the investigation of the biosensor under study for good sensing capabilities. These are the structural parameters: $\Lambda = 1\ \mu m$, $d_1/\Lambda = 0.30$, $d_0\Lambda = 0.55$, $d_2/\Lambda = 0.50$, $d_m/\Lambda = 0.60$, and $t_{Au} = 40$ nm.

The two large slots of the third ring are completely filled with an aqueous analyte with a refractive index of $n_a = 1.33$ and the confinement losses for the two polarized modes, HE^x_{11} and HE^y_{11} are solved. The steps are repeated for adifferent analyte with refractive index $n_a = 1.34$. The results for the two procedures are illustrated in Fig. 2. The plots in Fig. 2 shows loss spectra for both fundamental modes, HE^x_{11} and HE^y_{11}. The change in analyte refractive index from 1.33 to 1.34 causes the loss peak at resonance to shift (dashed curves). The peaks correspond to the phase matching points between the respective guided modes in the core and plasmon modes as illustrated in Fig. 2.

Fig. 3 shows the magnetic field distribution for both HE^x_{11} and HE^y_{11} (fundamental modes), near the region ofthe plasmonic peaks of the PCF SPR biosensor under study. Fig. 3 illustrates that there is relatively much leakage into the analyte filled slots for the case of HE^x_{11} in comparison to that of HE^y_{11}. This explains the relatively higher losses shown in Fig. 2

Like many other fiber based SPR sensors, the proposed sensor operates very near to the phase matching point when there is coupling of the core guided mode to the surface plasmon

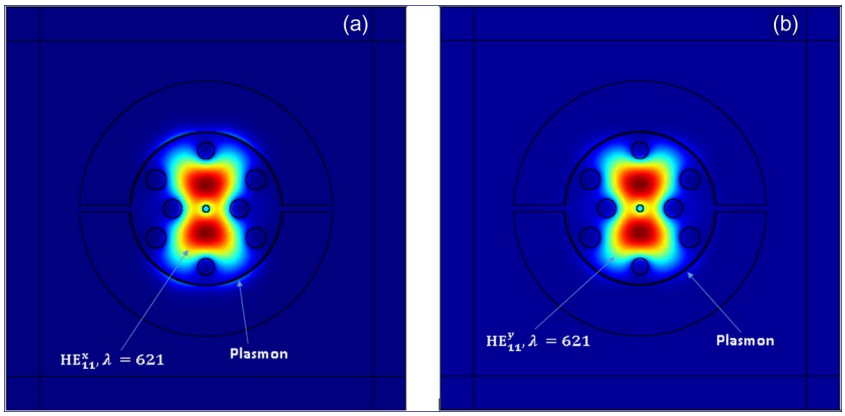

Fig. 3. The distribution (magnetic field) of polarized modes (a) HE_{11}^{x} and (b) HE_{11}^{y} close to the resonant wavelength when phases of SPP mode and core-guided mode are matched.

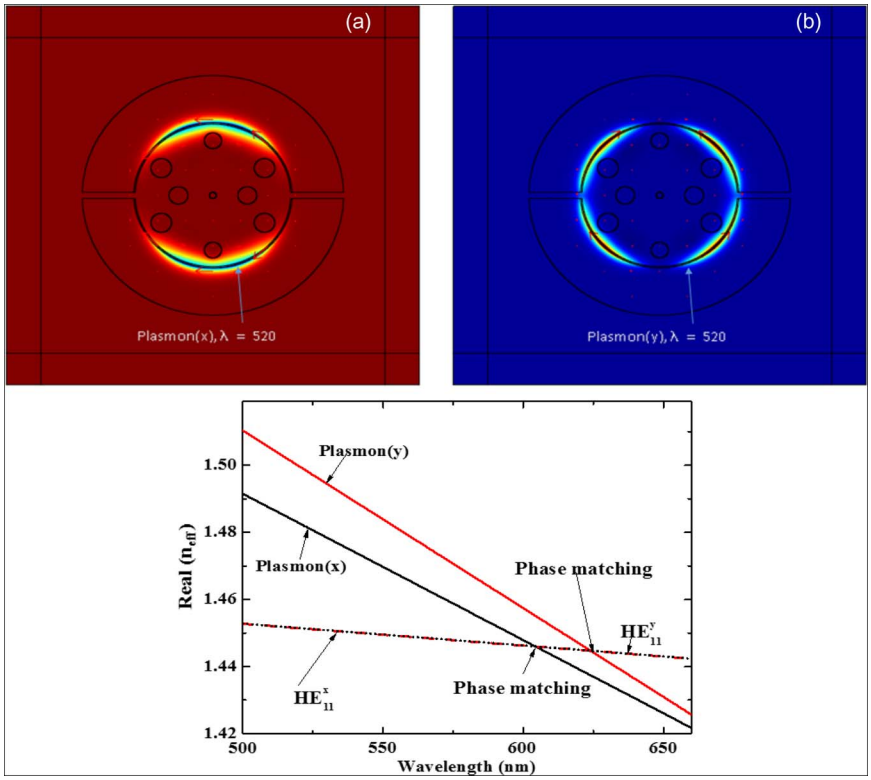

Fig. 4. Dispersion relationship of SPP mode (solid curve) and core-guided mode (dash curve) in the vicinity of the resonant wavelength when phases of SPP mode and core-guided mode are matched (a). The magnetic field distribution of plasmon mode (b).

wave propagating on the metal surface. Magnetic field profiles of the respective surface plasmons on the metal surface have been shown in Fig. 4(a) and (b). Fig. 4 also shows the dispersion relationship between the guided core mode (solid curves) and plasmon mode (dashed curves). It shows the phase matching points of the core-guided and plasmon modes for both x and y polarizations. The x-polarized fundamental core guided mode (HE_{11}^{x}) crosses the x-polarized plasmon wave (plasmon x) at approximately 604 nm while the y polarized fundamental core guided mode (HE_{11}^{y}) crosses the y-polarized plasmon wave(plasmon y) at approximately 624 nm. At these points, the refractive indices of a pair (plasmon and fundamental) are very close.

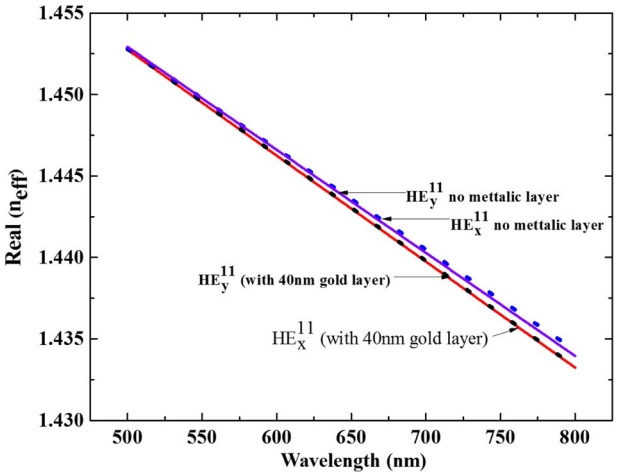

Fig. 5. Dispersion relationship of fundamental mode with and without a layer of metal.

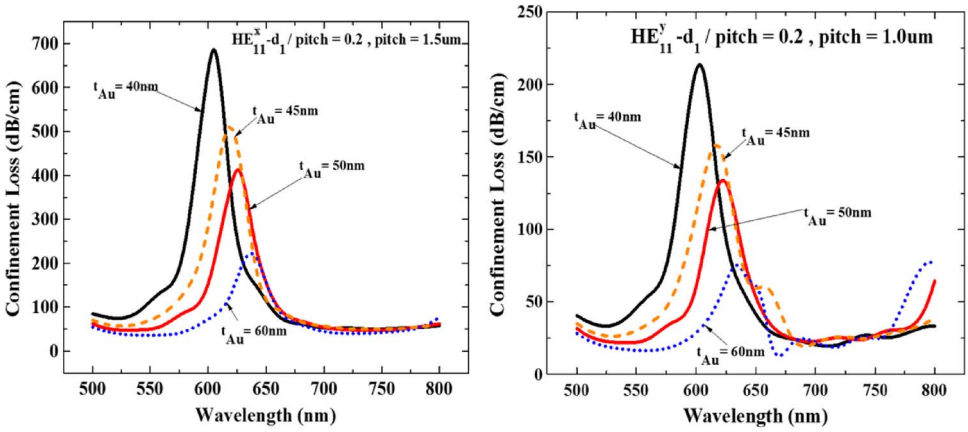

Fig. 6. Effect of variation of gold thickness on loss for proposed PCF biosensor. Refractive index of analyte $(n_a) = 1.33$.

Another compelling proof for the knowledge that there is coupling between the fundamental and plasmon modes at thephase matching point is featured in Fig. 5. It displays the dispersion relationship of the proposed plasmon biosensor with and without the gold layer. It is easily observed that the effective indices of the fundamental polarized modes for both setups are in close proximity [14].

Surface plasmon waves propagate along the metallized surface. Hence, the thickness of the metal layer affects theintensity of the surface excitations hence the sensitivity of the plasmon mode. We investigate the shifts in the plasmonic peak spectra by varying t_{Au} from 40 nm to 50 nm. The refractive index the analyte (1.33) together with all other structural variables are held constant for all variations in the thickness of the gold layer. The loss spectra for the fundamental polarized modes for each scenario are illustrated in Fig. 6. It is observed from Fig. 6 that there is a decrease in modal propagation loss as gold thicknessis varied from 40 nm to 50 nm.

Additionally, the resonant peak at the phase matching point shifts to higher wavelengths as t_{Au} increases. The relationship between resonant wavelength and metal layer thickness provides a way of studying interactions of nanoparticles on the metallic surface ofthe sensor [25]. A more practical approach would be its use in photodynamic cancer therapy [25].

The current design employs a central air hole to phase tune the plasmon mode to match that of the core guided mode. For this reason, the next phase of our study will investigate, the role of

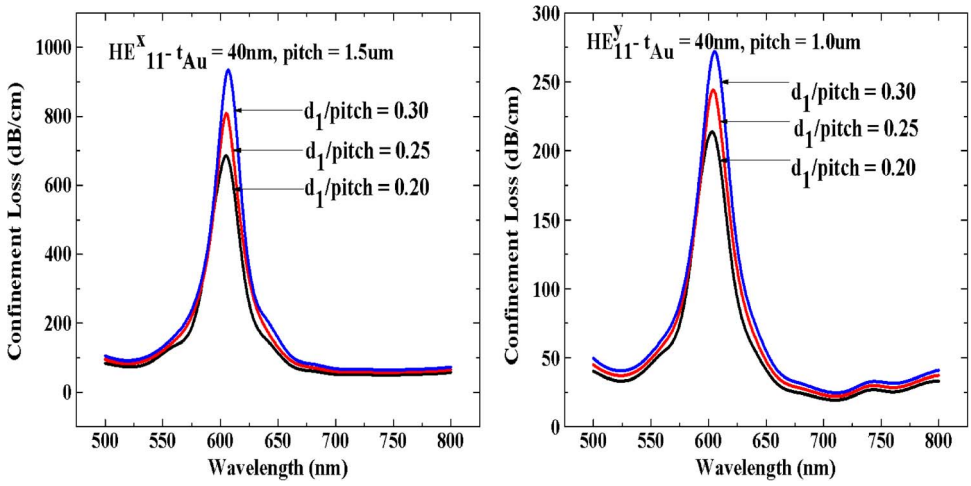

Fig. 7. Effect of variation of central hole diameter to pitch ratio on loss for the proposed PCF biosensor. Refractive index of analyte $(n_a) = 1.33$.

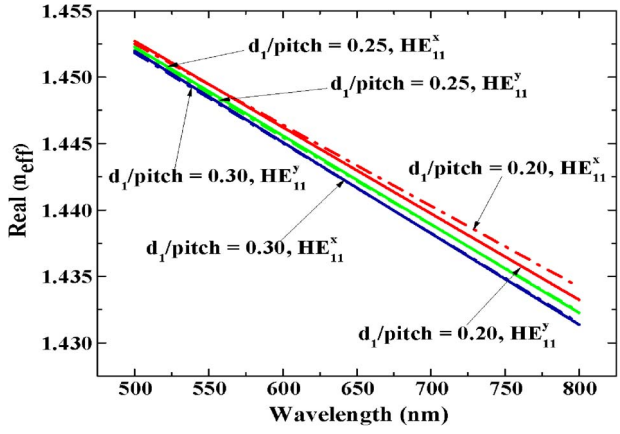

Fig. 8. Dispersion relationship of x and y polarizations of the core mode with variation in d_1. Refractive index of analyte $(n_a) = 1.33$.

d_1 in tuning and optimizing plasmon generation andcoupling with the guided modes in the core of the biosensor. This is achieved by varying d_1/Λ from 0.20 to 0.30 and calculating the loss spectra while keeping all other parameters constant.

Fig. 7 illustrates an overall appreciation in the modal loss of the two modes HE^x_{11} and HE^y_{11} as d_1/Λ takes on values from 0.20 to 0.30. The increasing modal losses are as a result of the guided core mode being pushed outward by the increasing central of airhole diameter, d_1, thereby increasing its mode presence close to the metallic surface resulting in larger propagation losses.

Additionally, it can be observed that the modal refractive index reduces, as shown in Fig. 8, as the core guided mode is pushed out from the central core region toward the metallized surface resulting in the shift of the plasmon peaks toward longer wave lengths (see Fig. 7).

3.1. Characterization of Sensor Sensitivity

The operation of most SPR sensors is based on the detection of change in the bulk refractive index of the analyte [1], [10], [25]. The analyte refractive index has a sturdy dependence on the real part of the complex refractive index of the plasmon wave. This makes coupling of the

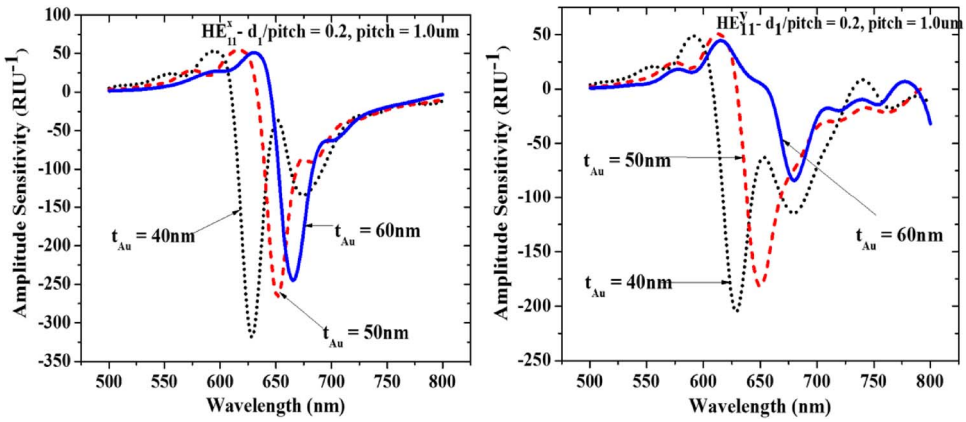

Fig. 9. Realationship between amplitude sensitivity and gold layer thickness of the PCF biosensor for varying t_{Au}.

guided-core mode with the plasmon at phase matching responsive to variations in the refractive index of the analyte [1], [25] The two main interrogation methods used are: amplitude or phase interrogation and wavelength or spectral interrogation. In amplitude interrogation, sensitivity is measured at a single wavelength, which makes this interrogation technique very low cost and simple since there is no need for spectral manipulation [1].

The demerit, however, is in its narrow operation scope and lower sensitivity as compared to spectral sensitivity [1], [25]. Amplitude sensitivity is given by [25]

$$S_A(\lambda) = -\left(\frac{\partial\alpha(\lambda, n)}{\partial n_a}\right) \Big/ \alpha(\lambda, n_a) \quad [\text{RIU}^{-1}] \tag{7}$$

where $\alpha(\lambda, n_a)$ is the attenuation of the core mode at a particular wavelength.

Fig. 9 illustrates the amplitude sensitivity of our bio-sensor for varyingthickness of gold. The HE^x_{11} mode registered a maximum value of 317 RIU[1] from Fig. 9 for $t_{Au} = 40$ nm. Similarly, a maximum sensitivity value of 205 RIU^{-1} is observed for HE^y_{11} mode, at $t_{Au} = 40$ nm. Sensor resolutions of 3×10^{-5} RIU and 4×10^{-5} RIU for HE^x_{11} and HE^y_{11}, respectively, are attained if it is assumed that a change of 1% in the transmitted intensity can be detected reliably.

Fig. 9 also describes the inverse relationship between sensitivity and goldlayer thickness. As the metal thickness increases (larger than skin depth, ~20–30 nm), there is less penetration of the core mode into the metal, resulting in weak coupling with surface plasmon modes, subsequently affecting the sensitivity. Despite this behavior, the HE^x_{11} mode records relatively higher sensitivity value as compared to that of the HE^y_{11} mode because its relatively higher mode presence in the metallic region.

In what follows, we proceed to investigate the sensitivity of the proposed sensor when operated in the wavelength interrogation mode. The sensitivity in this case is given as [1]

$$S_\lambda(\lambda) = \frac{\partial\lambda_{peak}}{\partial n_a} [\text{nm/RIU}] \tag{8}$$

where λ_{peak} represents the wavelength of the plasmonic peak at resonance condition. Shift in the plasmonic peaks for the loss spectra during variation int_{Au} is illustrated in Fig. 10. The maximum shift in $_{peak}$ for both HE^x_{11} and HE^y_{11} modes is 20 nm and 17 nm, respectively, at $t_{Au} = 40$ nm. This results in spectral sensitivities of 2000 nm/RIU and 1700 nm/RIU forHE^y_{11} and HE^y_{11} modes, respectively. Considering a 1% change in transmitted intensity, the spectral resolutions are 5×10^{-5} RIU for HE^x_{11} modes and 6×10^{-5} RIU for HE^y_{11} modes.

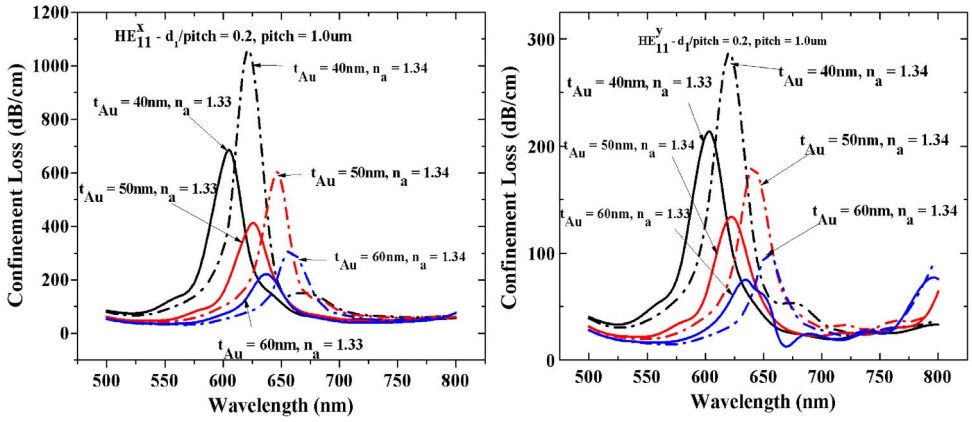

Fig. 10. Effect gold thickness and analyte refractive index on resonant wavelength of the PCF biosensor.

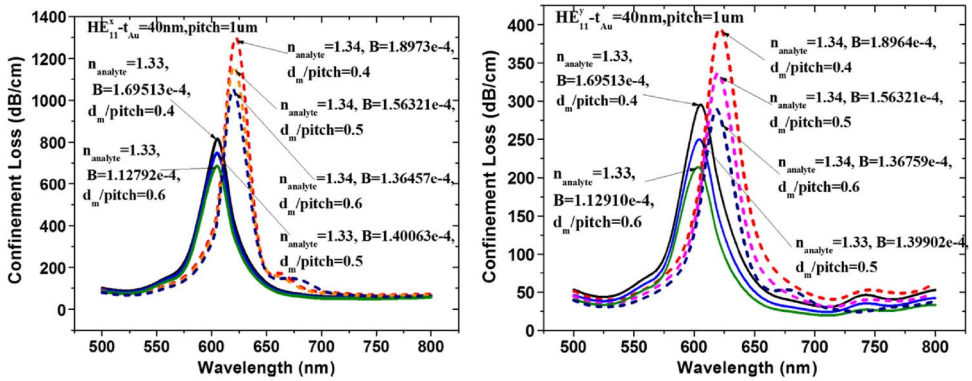

Fig. 11. Effect of variation of d_m/Λ on loss and birefringence for the proposed PCF biosensor. Refractive index of analyte $(n_a) = 1.33$.

To investigate the effect of birefringence on the spectral sensitivity, the parameter d_m/Λ is made to take on values from 0.40 to 0.60 without varying any of the other structural parameters. Loss spectra for all variations of d_m/Λ were plotted along with the birefringence values at resonance peaks for both fundamental modes 4 (HE_{11}^x and HE_{11}^y). Fig. 11 illustrates a general decrease in birefringence as d_m/Λ increases and resonant peaks shifting toward shorter wavelength. Modal losses of the two polarized modes (HE_{11}^x and HE_{11}^y) also decrease. This is because the coreguided mode is confined more to the core of the PCF. Fig. 11 also features a general decrease of spectral sensitivity as birefringence decreases resulting in the shifting of resonance peaks to shorter wavelengths for both fundamental modes (HE_{11}^x and HE_{11}^y). At $d_m/\Lambda = 0.40$ the maximum λ_{peak} change for HE_{11}^x mode is 17 nm with a birefringence of 1.69513×10^{-4} and 1.8973×10^{-4} calculated at the phase matching point for $n_a = 1.33$ and $n_a = 1.34$, respectively. While the maximum λ_{peak} change for HE_{11}^y mode is 16 nm with a birefringence of 1.69513×10^{-4} and 1.8964×10^{-4} calculated at the phase matching point for $n_a = 1.33$ and $n_a = 1.34$, respectively.

Furthermore, at $d_m/\Lambda = 0.60$, the maximum λ_{peak} change for HE_{11}^x mode is 15 nm with a birefringence of 1.12792×10^{-4} and 1.36457×10^{-4} calculated at the phase matching point for $n_a = 1.33$ and $n_a = 1.34$, respectively, whereas the maximum λ_{peak} change for HE_{11}^y mode at $d_m/\Lambda = 0.60$ is 15 nm with a birefringence of 1.1291×10^{-4} and 1.36759×10^{-4} calculated at the phase matching point for $n_a = 1.33$ and $n_a = 1.34$, respectively. These results show how the phase matching points and sensitivities can be tuned by varying d_m.

Analysis performed so far indicates that it is possible to optimize the structural parameters of the proposed sensorto realize different sensors of various lengths, taking into consideration the inverse law relationship between sensor length and modal losses.

The high losses at the plasmonic peaks of the proposed PCF SPR sensor limit it to the centimeter scale to enable easy detection of the signal. Such a structure is best considered as an integrated photonics element rather than a fiber. However, these losses can be reduced by optimizing structural parameters such as t_{Au}, d_m, and d_1 as discussed in the previous sections. There must, however, be a compromise between high sensitivity and low losses.

The analysis presented so far indicate the possibility of realizing a PCF SPR sensor with differential sensitivities as far as the fundamental modes HE_{11}^x and HE_{11}^y are concerned. There is the possibility of optimizing d_1 and d_m to obtain substantial difference in the respective sensitivities of HE_{11}^x and HE_{11}^y modes. This particular feature will beuseful in applications where simultaneous observation of both bulk and surface contributions to sensor response is required and also multi analyte/multi-channel sensing. Some researchers have successfully demonstrated both theoretically and experimentally the importance of such a feature in SPR biosensors [30]–[32].

4. Conclusion

A detailed theoretical study of a novel PCF SPR biosensor has been presented in this paper. The biosensor structure is made up of a combination of microfluidic channels, waveguide and metallized layers making this design compact, in contrast to other common SPR biosensors. The coupling conditions at resonance, sensitivity, and loss spectra of this SPR based PCF biosensor have been investigated using a finite element method with perfectly matched layers. Furthermore, it has been demonstrated that the proposed sensor has differential sensitivity as far as the fundamental modes HE_{11}^x and HE_{11}^y are concerned and can be useful for multi analyte or multi-channel sensing and simultaneous detection of bulk and surface sensitivities. Simulations took into consideration the operation of the sensor in both spectral and amplitude interrogation modes. Characteristic sensor resolution values of 5×10^{-5} RIU and 6×10^{-5} RIU for HE_{11}^x and HE_{11}^y, respectively, were recorded for the spectral interrogation mode, while 3×10^{-5} RIU for HE_{11}^x modes and 4×10^{-5} RIU for HE_{11}^y modes, when the sensor was operated in the amplitude interrogation mode. The resolutions obtained are comparable to reported designs in [4] and [5]. Fabrication of the structure should not be much of a problem due to the few air holes and large channels for housing the analyte. The thin gold layer on the inner surfaces of the micro fluidicslots can be achieved using high pressure chemical vapor deposition technique, thermal evaporation or a sputtering method [26]. Alternatively, electroless plating techniques used in fabrication of metallized hollow waveguides and microstructures can also be employed to deposit required amount of gold [27], [28].

References

[1] J. Homola, S. S. Yee, and G. Gauglitz, "Surface plasmon resonance sensors: Review," *Sensors Actuators B. Chem.*, vol. 54, No. 1, pp. 3–15, 1999.
[2] E. K. Akowuah, T. Gorman, S. Haxha, and J. V. Oliver, "Dual channel planar waveguide surface plasmon resonance biosensor for an aqueous environment," *Opt. Exp.*, vol. 18, No. 24, pp. 24412–24422, Nov. 2010.
[3] E. K. Akowuah, T. Gorman, and S. Haxha, "Design and optimization of a novel surface plasmon resonance biosensor based on Otto configuration," *Opt. Exp.*, vol. 17, No. 26, pp. 23511–23521, Dec. 2009.
[4] W. Qin, S. Li, Y. Yao, X. Xin, and J. Xue, "Analyte-filled core self-calibration microstructured optical fiber based plasmonic sensor for detecting high refractive index aqueous analyte,"*Opt. Lasers Eng.*, vol. 58, pp. 1–8, Jul. 2014.
[5] J. N. Dash and Jha, "SPR biosensor based on polymer PCF coated with conducting metal oxide," *IEEE Photon. Technol. Lett.*, vol. 26, no. 6, pp. 595–598, Mar. 2014.
[6] T. T. Goodrich, H. J. Lee, and R. M. Corn, "Direct detection of genomic DNA by enzymatically amplified SPR imaging measurements of RNA microarrays," *J. Am. Chem. Soc.*, vol. 126, no. 13, pp. 4086–4087, Apr. 2004.
[7] J. Homola, H. Vaisocherová, J. Dostálek, and M. Piliarik, "Multi-analyte surface plasmon resonance biosensing," *Methods*, vol. 37, no. 1, pp. 26–36, Sep. 2005.

[8] R. Jha and A. K. Sharma, "High-performance sensor based on surface plasmon resonance with chalcogenide prism and aluminum fordetection in infrared," *Opt. Lett.*, vol. 34, no. 6, pp. 749–751, Mar. 2009.
[9] K. Wang *et al.*, "High-sensitivity electro-optic-modulated surface plasmon resonance measurement using multilayer waveguide-coupled surface plasmon resonance sensors," *Sensor Lett.*, vol. 8, no. 2, pp. 370–374, Apr. 2010.
[10] M. Piliarik, L. Párová, and J. Homola, "High-throughput SPR sensor for food safety." *Biosensors Bioelectron.*, vol. 24, no. 5, pp. 1399–1404, Jan. 2009.
[11] R. Jorgenson and S. Yee, "A fiber-optic chemical sensor based on surface plasmon resonance," *Sensors Actuators B. Chem.*, vol. 12, no. 3, pp. 213–220, Apr. 1993.
[12] D. Monzón-Hernández and J. Villatoro, "High-resolution refractive index sensing by means of a multiple-peak surface plasmon resonance optical fiber sensor," *Sensors Actuators B. Chem.*, vol. 115, no. 1, pp. 227–231, May 2006.
[13] H. Suzuki, M. Sugimoto, Y. Matsui, Y. J. Kondoh, "Fundamental characteristics of a dual-colour fibre optic SPR sensor," *Meas. Sci. Technol.*, vol. 17, no. 6, pp. 1547–1552, 2006.
[14] E. K. Akowuah, H. Ademgil, S. Haxha, G. K. Robinson, and J. V. Oliver, "Numerical analysis of a photonic crystal fiber for biosensing applications," *IEEE J. Quantum Electron.*, vol. 48, no. 11, pp. 1403–1410, Nov. 2012.
[15] S. Patskovsky, M. Meunier, N. P. Prasad, and V. A. Kabashin, "Self-noise-filtering phase-sensitive surface plasmon resonance biosensing," *Opt. Exp.*, vol. 18, no. 14, pp. 14353–14358, Jul. 2010.
[16] X. Hoa, A. Kirk, and M. Tabrizian, "Towards integrated and sensitive surface plasmon resonance biosensors: A review of recent progress," *Biosensors Bioelectron.*, vol. 23, no. 2, pp. 151–160, Sep. 2007.
[17] A. Dhawan, M. D. Gerhold, and J. F. Muth, Plasmonic structures based on subwavelength apertures for chemical and biological sensing applications. *IEEE Sensors J.*, vol. 8, no. 6, pp. 942–950, Jun. 2008.
[18] A. Ferrando, E. Silvestre, J. J. Miret, P. Andres, and M. Andres, "Vector description of higher-order modes in photonic crystal fibers," *J. Opt. Soc. Amer. A*, vol. 17, no. 7, pp. 1333–1340, Jul. 2000.
[19] F. Zolla *et al.*, *Fundamentals of Photonic Crystal Fibers*. London, U.K.: Imperial College, 2005.
[20] H. Ademgil, S. Haxha, T. Gorman, and F. AbdelMalek, "Bending effects on highly birefringent photonic crystal fibers with low chromatic dispersion and low confinement losses," *IEEE, J. Lightw. Technol.*, vol. 27, no. 5, pp. 559–567, Mar. 2009.
[21] Y. Du, *et al.*, "Polarization splitting filter characteristics of Au-filled high-birefringence photonic crystalfiber," *Appl. Phys. B*, vol. 109, no. 1, pp. 65–74, Oct. 2012.
[22] B. Gauvreau, A. Hassani, M. F. Fehri, A. Kabashin, and M. Skorobogatiy, "Photonic bandgap fiber-based surface plasmon resonance sensors," *Opt. Exp.*, vol. 15, no. 18, pp. 11413–11426, Sep. 2007.
[23] A. Hassani and M. Skorobogatiy, "Design of the microstructured optical fiber-based surface plasmon resonance sensors with enhanced microfluidics," *Opt. Exp.*, vol. 14, no. 24, pp. 11616–11621, Nov. 2006.
[24] M. Hautakorpi, M. Mattinen, and H. Ludvigsen, "Surface-plasmon-resonance sensor based on three-hole microstructured optical fiber" *Opt. Exp.*, vol. 16, no. 12, pp. 8427–8432, Jun. 2008.
[25] A. Hassani, B. Gauvreau, M. F. Fehri, A. Kabashin, and M. Skorobogatiy, "Photonic crystal fiber and waveguide-based surface plasmon resonance sensors for application in thevisible and near-IR," *Electromagnetics*, vol. 28, no. 3, pp. 198–213, 2008.
[26] P. J. Sazio *et al.*, "Microstructured optical fibers as high-pressure microfluidic reactors," *Science*, vol. 311, no. 5767, pp. 1583–1586, 2006.
[27] J. A. Harrington, "A review of IR transmitting, hollow waveguides," *Fiber Integr. Opt.*, vol. 19, no. 3, pp. 211–227, 2000.
[28] N. Takeyasu, T. Tanaka, and S. Kawata, "Metal deposition deep into microstructure by electroless plating," *Japanese J. Appl. Phys.*, vol. 44, no. 8L, pp. L1134, 2005.
[29] K. Saitoh, M. Koshiba, T. Hasegawa, and E. Sasaoka, "Chromatic dispersion control in photonic crystal fibers: Application to ultra-flattened dispersion," *Opt. Exp.*, vol. 11, no. 8, pp. 843–852, 2003.
[30] E. K. Akowuah *et al.*, "Novel compact photonic crystal fibre surface plasmon resonance biosensor for an aqueous-senvironment," in *Photonic Crystals–Innovative Systems, Lasers and Waveguides*. Winchester, U.K.: Intech, pp. 81–96, 2012, ch. 6.
[31] W. Sellmeier, "Zur erklärung der abnormen farbenfolge im spectrum einiger substanzen," *Annalen der Physik und Chemie*, vol. 219, no. 6, pp. 272–282, 1871.
[32] Y. Y. Shevchenko and J. Albert, "Plasmon resonances in gold-coated tilted fiber Bragg gratings," *Opt. Lett.*, vol. 32, no. 3, pp. 211–213, Feb. 2007.
[33] Y. Shevchenko, C. Chen, M. A. Dakka, and J. Albert, "Polarization-selective grating excitation of plasmons in cylindrical opticalfibers," *Opt. Lett.*, vol. 35, no. 5, pp. 637–639, Mar. 2010.
[34] C. Caucheteur, Y. Shevchenko, Y. L. Shao, M. Wuilpart, and J. Albert, "High resolution interrogation of tilted fiber grating SPR sensors from polarization properties measurement," *Opt. Exp.*, vol. 19, no. 2, pp. 1656–1664, Jan. 2011.